Received: 11 May 2022 | Revised: 29 July 2022 | Accepted: 30 July 2022

DOI: 10.1049/nbt2.12095

IET Nanobiotechnology

The Institution of Engineering and Technology WILEY

ORIGINAL RESEARCH

Functional characteristics of the rigid elytra in a bamboo weevil beetle *Cyrtotrachelus buqueti*

Xin Li | **Yu Zheng**

College of Mechanical and Electrical Engineering, Suqian University, Suqian, China

Correspondence

Xin Li, College of Mechanical and Electrical Engineering, Suqian University, Suqian, China.
Email: nanlixin@nuaa.edu.cn

Funding information

The Natural Science Foundation of Jiangsu Higher Education Institutions of China, Grant/Award Number: 21KJD460002; The Suqian Sci&Tech Program of China, Grant/Award Number: K202115; The Research and Design Innovation Team of Lightweight Rotor Pump of Suqian University, Grant/Award Number: 2021td7

Abstract

The bamboo weevil beetle, *Cyrtotrachelus buqueti*, has evolved a particular flight pattern. When crawling, the beetle folds the flexible hind wings and stuffs under the rigid elytra. During flight, the hind wings are deployed through a series of deployment joints that are passively driven by flapping forces. When the hind wings are fully expanded, the unfolding joint realises self-locking. At this time, the hind wings act as a folded wing membrane and flap simultaneously with the elytra to generate aerodynamics. The functional characteristics of the elytra of the bamboo weevil beetle were investigated, including microscopic morphology, kinematic properties and aerodynamic forces of the elytra. In particular, the flapping kinematics of the elytra were measured using high-speed cameras and reconstructed using a modified direct linear transformation algorithm. Although the elytra are passively flapped by the flapping of the hind wings, the analysis shows that its flapping wing trajectory is a double figure-eight pattern with flapping amplitude and angle of attack. The results show that the passive flapping of elytra produces aerodynamic forces that cannot be ignored. The kinematics of the elytra suggest that this beetle may use well-known flapping mechanisms such as a delayed stall and clap and fling.

KEYWORDS

3D reverse reconstruction, aerodynamic force, bio-inspired structures, microstructure, wing kinematics

1 | INTRODUCTION

Insects show fascinating agility when they are flying against the wind, chasing prey, landing accurately and avoiding natural enemies, which benefits from the ingenious airfoil structure and unique kinematic characteristics of insect wings. The aerobatic flight completed by insects not only relies on their neurosensory-motor control system to make accurate and rapid responses but also requires wings to flexibly change different flight modes. In view of the special background of military reconnaissance, disaster relief and rescue, deep space exploration and intelligence collection, insect-like flying robot highlights its important application value. Therefore, the morphology of insect wings provides help to study the kinematics of wings, and the kinematic laws of wings provide theoretical models for understanding the aerodynamic generation of insect flapping wings.

In recent years, people have carried out in-depth research on the aerodynamic characteristics of insect flight [1–7]. Mechanisms such as delayed stall, advanced rotation, rotational lift, wake capture, clap and fling, figure-eight motion and wing interaction have now been accepted [8]. The complex control of the wing kinematics of insects enables the generation of unsteady aerodynamic forces and can provide source data for the design and flight testing of small aircraft. The flying robot is designed to imitate the flight characteristics of the bumblebee, and the driving structure is prepared by adding piezoelectric material into the intelligent composite structure [9]. The composite bionic flapper was designed by imitating the wing structure of *Nephrotoma appendiculata*. The wing veins were made of 'SU-8' material and the wing membrane was made of Polydimethylsiloxane [10]. The coaxial quad-wing flapper was designed by imitating the flapping wing characteristics of butterflies, and its aerodynamic mechanism was investigated by the computational fluid dynamics (CFD) simulation and a wind tunnel experiment [11]. A tiny robot that can fly in the air, hover, land on land, swim in water, and jump out of water has been designed [12]. A flying robot that can

accurately simulate the fast escape action of fruit flies has been developed by imitating the flight characteristics of fruit flies [13].

Compared with the flight mechanism of other insects, the wing kinematics of the beetle has received little attention due to the difficulty of the experimental operation and the limited valuable wing behaviour data obtained in the beetle flight. Wind tunnel experiments and CFD simulators from ANSYS-CFX software were used to study the aerodynamic properties and force generation mechanisms of the *Allomyrina dichotoma* beetle, and it was found that the elytra produced less than 1% of its body weight in lift [14]. Quantitative measurements of beetle *Heliocopris hamadryas* wakes show that the presence of elytra helps support body weight and increases vertical force production by approximately 40%, and that the combination of elytra and hindwing produces a complex wake [15]. Airflow characteristics around the elytra and hindwings of the *Trypoxylus dichotomus* beetle were observed by using the smoke-wire visualisation technique [16]. It was revealed that the increased suction in the gap between the elytra and the hindwing may increase the lift on the hindwing during the upstroke. The kinematics and deformation behaviour of *T. dichotomus* beetle's hind wing were measured by the motion capture system, and the mechanism of beetle's forward flight and the aerodynamic force acting on the elytra were discussed by numerical simulation [17, 18]. The SST k-ω turbulence model based on three-dimensional (3D) pressure simulation was used to analyse the take-off and landing performance of the *Rhinoceros* beetle in detail [19]. Numerical simulation was used to explore the influence of the microstructure of the elytra and the blood flow in hind wing veins on the aerodynamic force of the beetle [20]. The fluid structure of clap and fling effect and force generation in the *A. dichotoma* beetle is investigated by simulation [21]. In-flight collisions of wings imitating the curved joints of the hindwings found that the origami-like folds of *A.* beetles' hindwings played an important shock-absorbing function in the collision of the hindwings in flight [22].

The bamboo weevil beetles, *Cyrtotrachelus buqueti*, may have excellent flight mobility [23, 26]. It has a wing load-carrying capacity of 79 N/m^2 [25], which is higher than that of *A. dichotoma* (40 N/m^2), the fruit fly (2 N/m^2) and the dragonfly (7.5 N/m^2). Moreover, the folding ratio of the hind wings of *C. buqueti* is larger than that of *A. dichotoma* and *Pachnoda marginata* beetles, which belong to the secondary folding and unfolding mechanism. The weight of adult *C. buqueti* is more in line with the miniaturised biomimetic goal of flapping-wing micro air vehicles (MAVs). The functional morphological and structural characteristics of the hind wings of *C. buqueti* were studied, and it was found that resilin located in a specific area of the hind wings could avoid the fatigue damage of the hind wings and contribute to the folding and unfolding motion of the wings [23]. The microstructure shows that the hind wing is a layered structure with filaments, which makes the hind wing lightweight and highly flexible. Moreover, mechanical tests found that the bending stiffness in the chordwise direction was higher than that in the spanwise direction, which was determined by the distribution characteristics of the fibre layers in the hind wing [24]. The static characteristics and natural vibration modes of the hind wing structure are analysed by the finite element method. The small deflection under uniformly distributed load and bending moment shows that the hind wing of *C. buqueti* has excellent structural performance [25]. The flapping pattern of the double figure-eight trajectory creates the excellent flight manoeuverability of *C. buqueti* [26]. The folding mechanism, kinematic data and morphological parameters of the wing of *C. buqueti* are simulated to design the deployable mechanism, and its rigid–flexible coupling dynamic characteristics of folding and unfolding are analysed. Furthermore, a flapping-wing MAV with a foldable mechanism was designed and the load-bearing capacity and vibration mode of the wing were analysed by the finite element method [27]. These studies provide important references for the development of beetle-like flapping-wing MAVs with foldable wings.

Further research found that before flight, *C. buqueti* opens its elytra and then unfolds its hind wings. The flapping of the hind wings is actively controlled by the muscles at the root of the wings. Although the muscles at the wing root of *C. buqueti* do not control the flapping motion of the elytra, it is achieved by passive flapping through the movement of the hind wings. However, the approximation between the elytra and hind wings of *C. buqueti* in flight suggests that their interactions may have important effects on aerodynamic performance. Therefore, this article focusses on the functional properties of the elytra of *C. buqueti*, including its morphological properties, kinematic properties of passive flapping and aerodynamic generation. The cross-sectional structure of the hind wing was observed by the scanning electron microscope and its average thickness was obtained. The elytra were scanned with a 3D scanner, and their 3D model was reconstructed. The position angle, the rotation angle and the elevation angle data of flapping wing motion are obtained by processing the high-speed video frames. Fourier series were used to fit these angular data to construct a kinematic model of *C. buqueti* flapping wings. The airflow characteristics around the elytra are analysed using CFD simulations. The research in this study will provide a good reference for a more in-depth study of the aerodynamics of the elytra-hind wing coupling characteristics of *C. buqueti*.

2 | EXPERIMENTAL METHODS

2.1 | Tested samples

We prepared about 20 *C. buqueti* specimens. The test specimens were taken from adult *C. buqueti* captured in *Suqian* city, *Jiangsu Province*, China in 2021, with an average mass of 3.28 g. Several live individuals with similar morphology and same mass were taken for kinematic measurement. The elytra were cut from the body and stored in a container at a room temperature of 26°C and humidity of 60% for scanning electron microscopy (SEM) observation and 3D scanning.

2.2 | Scanning electron microscopy

The cross section and ventral side microstructure of the elytra were observed by SEM. The elytra samples were cleaned with 0.10 mol/L phosphate buffer for 15 min and dehydrated using ethanol. Cutting the elytra with a blade destroys the microstructure of its cross section. To make the test samples extremely fragile, the dehydrated elytra were immersed in liquid nitrogen for 8 min, and then the elytra were broken by hand along the middle of the wing chordwise direction. The samples were mounted on a SEM stage with graphite adhesive tape, and the fractured cross sections of the samples were coated with gold-palladium. To avoid the surface impurities of the test sample affecting the observation results, the nozzle of the compressed air tank is used to remove dust from the samples on the stages. Finally, the microstructure of the elytra was observed and measured using SEM (Quanta200, FEI, USA) at an accelerating voltage of 20 kV.

2.3 | High-speed photography

To measure the 3D flapping patterns of *C. buqueti*, a motion capture system consisting of a projection lamp and three high-speed cameras distributed around a customised studio frame, a motion plane with sensors, a data processing system and a signal transmission device was used. The custom frame was covered with a blackout curtain to prevent noise and disturbance from external light during the experiments. The three high-speed cameras (Olympus, i-SPEED 3, Japan) operate with the computer to capture images simultaneously at 2000 fps with a spatial resolution of 1280 × 1024 pixels. Considering the typical flapping frequency of beetles' hindwings (30–70 Hz), the frame frequency of the cameras was set to be sufficient to measure several flapping cycles of the elytra. The calibration of the cameras and the experimental procedures of fixing the live specimens on the sensor are described in Ref [26, 27].

2.4 | 3D scanning

To analyse the flapping characteristics of the elytra of *C. buqueti*, the 3D model of *C. buqueti* should be reconstructed by reverse modelling technology to describe the kinematic characteristics of the elytra. One specimen was randomly selected from some surviving specimens with similar body weight and morphological parameters [24]. The elytra were separated from the wing root, and the sample was cleaned with distilled water and allowed to dry naturally at room temperature. To reduce the interference of laser data caused by the difference in reflectivity, colour and curvature characteristics of the surface of the sample during 3D scanning, the imaging agent (JIP145, Japan) was gently sprayed onto the surface of the hind wing to achieve a colouring effect. The elytra were scanned from the dorsal side to ventral side using a 3D scanner (JTscan-MS-50, China) to obtain point cloud data, as shown in Figure 1.

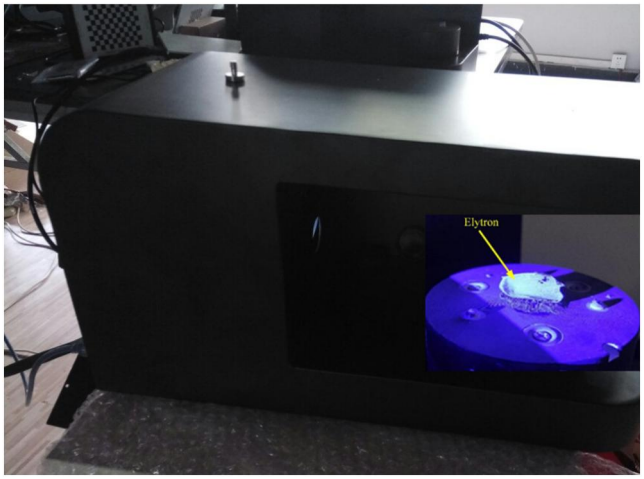

FIGURE 1 3D Scanning of the elytron

3 | RESULTS AND DISCUSSION

3.1 | Microstructure observation

The cross section of an elytron was obtained at 50% of the spanwise length. The microstructure of the cross section and ventral side surface (inner surface) of the elytra was observed by SEM. As shown in Figure 2, the cross-sectional morphology of the elytra is a sandwich-like hierarchical structure with dense filaments in each layer. Long holes are distributed in parallel along the wing spanwise direction of the elytra, and the holes of the hollow structure may enhance the impact resistance of the elytra and reduce the flight load of *C. buqueti*. The cross section of the elytron has a camber, and there are corrugations in the dorsal side surface (upper surface). The camber and local corrugation may have a significant effect on the aerodynamics of the elytra during the flapping motion. The microstructure of the ventral side observed densely sharp protrusions near the wing tips. First, the sharp protrusions can prevent the rear wing from popping out due to the stored elasticity of resilin during folding, which plays the role of interlock. Second, the sharp protrusions can increase the friction between the hind wings and the elytra and reduce the number of reciprocating brushings of the abdomen, which helps reduce the power consumption of *C. buqueti*. Third, when *C. buqueti* falls from the air, the sharp micro-protrusions may weaken the impact between the elytra and the hind wings.

Considering that in micrometre-scale samples, the small errors in the measured sample thickness can cause significant differences in mechanical properties, and marking the thickness of elytra by SEM can reduce measurement errors. The elytra of *C. buqueti* are relatively thin. While observing the microstructure with SEM, the size of the cross-sectional microstructure of the sample is measured more accurately based on the high-precision measurement function of SEM. The average thickness of the elytra was 15 μm from

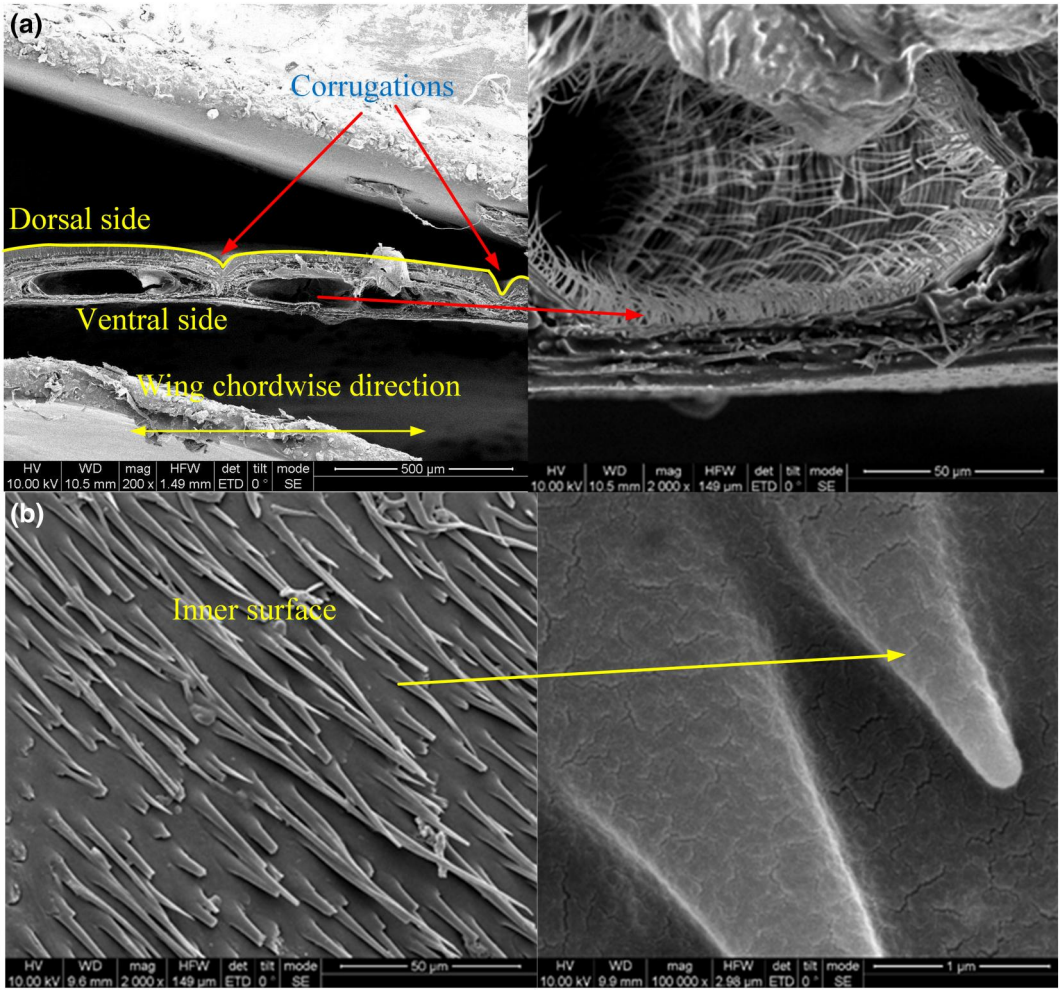

FIGURE 2 Microstructure of the cross section and inner surface of the elytra: (a) microstructure along the wing chordwise direction and (b) the sharp protrusions distributed on the inner surface of the elytra

multiple measurements. The measured thickness data contributes to the reverse reconstruction of the 3D model of the elytra.

3.2 | 3D reconstruction

The point cloud data of elytra were obtained by 3D scanning technology. In reverse engineering Imageware software, the noise points in the point cloud map of the elytra were removed and the point cloud data was simplified. The Gaussian filter is used to smooth the point cloud, and the dimensionality reduction of the point cloud is performed based on the chordal deviation method. The reverse modelling of the elytra surface was carried out using the point cloud fitting surface method. The reconstructed surface model is imported into Unigraphics NX software for surface merging and thickening. The reconstruction of the 3D geometric model of the elytron was completed, as shown in Figure 3. To accurately simulate the aerodynamic analysis of the flapping of the elytra, the thickness value of the elytra model is the average thickness measured by SEM in the thickening operation.

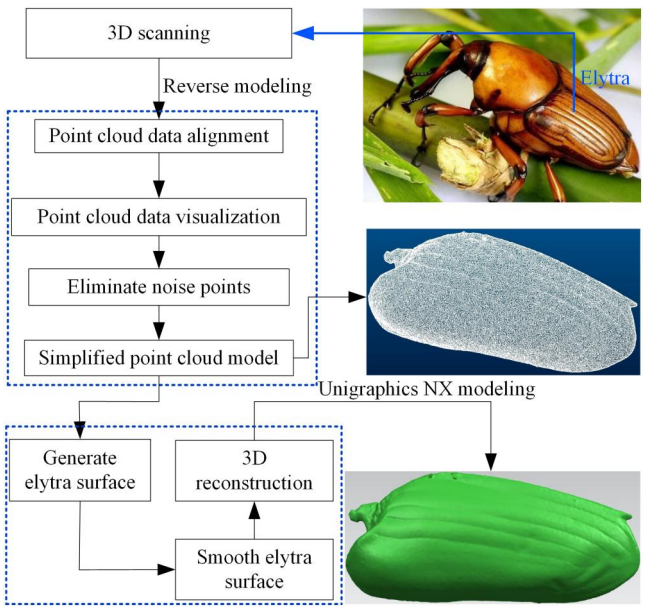

FIGURE 3 3D reconstruction process of the point cloud data of the elytron

3.3 | Kinematic properties of elytra flapping

To facilitate the wing kinematic modelling of the measured flapping behaviour of the elytra from the video frames, a reference coordinate system and the Euler angle describing the motion of the elytra are defined, as shown in Figure 4. The stroke plane is determined by the stroke plane angle β relative to an axis perpendicular to the longitudinal axis of *C. buqueti*. The deviation angle $\phi(t)$ is defined as the angle between the line connecting the wing base and the wing tip and its projection on the stroke plane. The flapping angle $\theta(t)$ is defined as the angle between the line connecting the wing base and the wing tip and its projection on the horizontal plane. The flapping angle $\theta(t)$ and the angle of attack $\alpha(t)$ are defined as the angle between the line connecting the wing base and the wing tip and its projection on the horizontal plane and the angle between the local chord and the horizontal plane, respectively. The angle between the longitudinal axis of the body and the horizontal plane is defined as body angle ε.

To track a specific point on the elytra, we need to mark the location to be detected. Hard markings such as thin metal films and small paint droplets are not used on elytra. The fluorescent dot markers, which are morphologically discernible features, were used to allow *C. buqueti* beetles fly without external disturbances. Considering that the elytra are different from the flexible hind wing, three fluorescent spots are marked at the wing tip, wing root and 50% of the wing spanwise length. Among several techniques developed for reconstructing 3D wing kinematics, a modified direct linear transform (DLT) algorithm and visual image correlation methods are used [28, 29]. The 3D positions of the fluorescent marks on the elytra were obtained from the geometric position of marker points through frame-by-frame analysis of the video. Video editing software AVIedit 3.39 and image measurement software Sigma Scan Pro v5.0 were used to process video frames.

The high-speed camera observed that the elytra of *C. buqueti* also flapped passively along with the flapping wing motion of the hind wings. The duration of pronation and supination during elytra flaps are approximately equal. The elytra rotate a relatively modest angle, about 10°, during pronation and supination. There were 29 frames for a single stroke, which means that the frequency of the elytra was 67 Hz ± 0.3 Hz. The elytra of the dung beetle *H. hamadryas* showed better aerodynamic performance when the wing beat frequency was 40 Hz [15]. Therefore, the contribution of the wing beat frequency of the elytra to the stable flight of *C. buqueti* cannot be ignored. The elytra and the hind wings are always flapping synchronously in all wing beat cycles. The high-speed camera captured the forward flight velocity of *C. buqueti* was about 2 m/s with zero degree of body angle. The flapping wing characteristic of the elytra is a double figure-eight trajectory pattern, which is similar to the wing-flapping trajectory of the hind wings [26], as shown in Figure 5. The crossing of a figure-eight shape occur near both pronation and supination in the flapping wing trajectory curves, which determines the flapping pattern and aerodynamic performance of insects [30, 31]. The intersection phenomenon is determined by the twisting behaviour of the elytra upstroke to the highest point and downstroke to the lowest point.

The flapping kinematics of the elytra of *C. buqueti* can be described by Euler angles $\phi(t)$, θ(t) and α(t), and the variation of the average angle of the five beetles is shown in Figure 6. The accurate kinematic parameters of insect wings can provide important data for the design of bionic wings and their flapping flight studies. Moreover, the flapping wing test of robotic wing is helpful to study the flight mechanism of insects, which in turn guides the optimal design of flapping wing MAV. Moreover, the flapping test of designing insect-like robotic wings helps to study the flight mechanism of insects, which in turn guides the optimal design of flapping-wing MAVs. It is

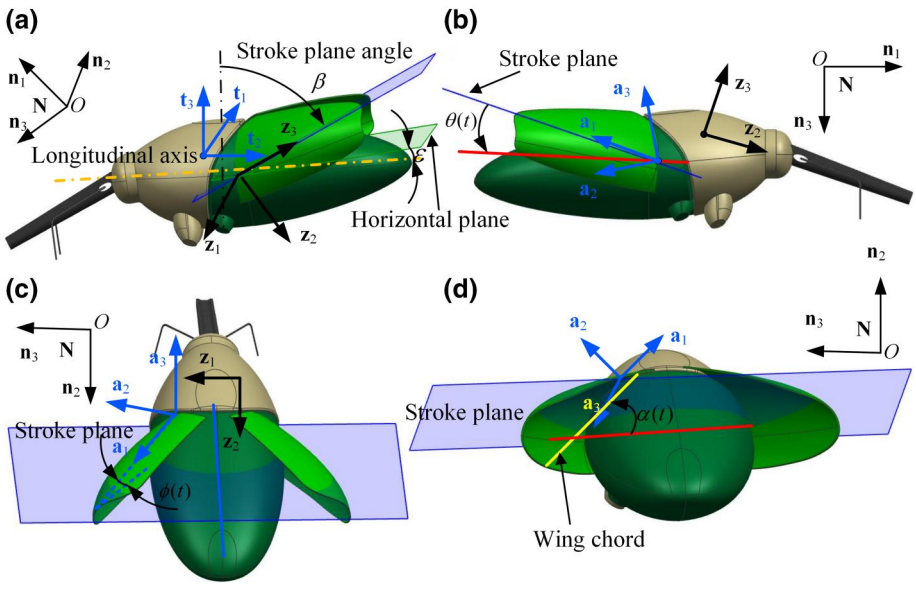

FIGURE 4 Wing kinematics description based on Euler angles. (a) The stroke plane angle β, (b) the flapping angle $\theta(t)$, (c) the deviation angle $\phi(t)$, and (d) the angle of attack $\alpha(t)$

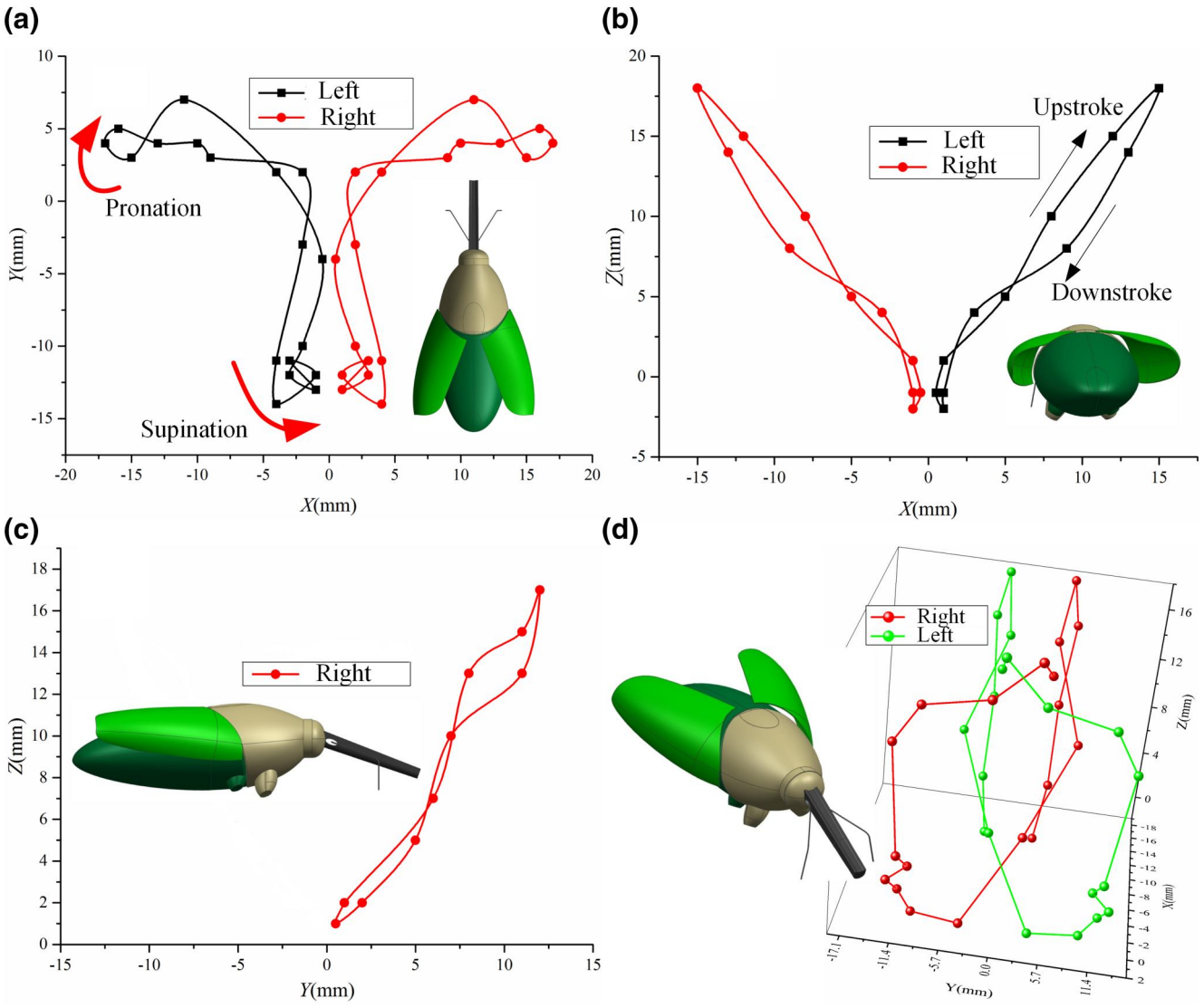

FIGURE 5 The flapping pattern of the elytra. (a) Flapping pattern of elytra photographed from top view, (b) flapping pattern of elytra photographed from the front view, (c) flapping pattern of elytra photographed from the side view, and (d) flapping trajectory of elytra in the 3D view

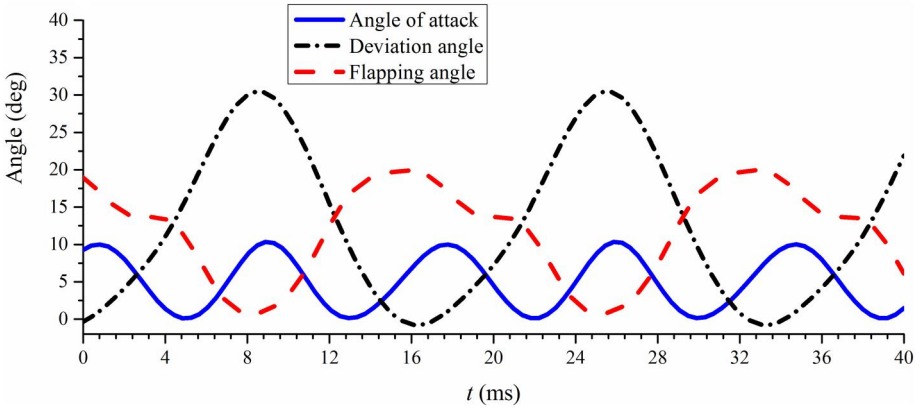

FIGURE 6 Average angle curves of the five samples during flapping motion

currently difficult to obtain detailed information on the pressure distribution of flapping wings experimentally, and it is impossible to obtain reliable estimates of the transient aerodynamic forces of insect flapping wings through momentum or velocity analysis [32]. Therefore, it is very important to accurately obtain the morphological parameters and kinematic equations of wings. Compared with the hind wings, the flapping angle of elytra is small but not negligible. Therefore, the aerodynamic force generated by the flapping of the elytra may be coupled with the aerodynamic force generated by the flapping of the hind wings to complete the flight mission. To explore the aerodynamic contribution of elytra flaps, the kinematic equations of elytra flaps need to be accurately established. Fourier coefficients have a good application in data fitting of insect flapping angles [11, 17, 33]. The fitted curve can intuitively reflect the variation law of flapping angle, which facilitates the input of calculation functions during numerical simulation. The general definition of Euler angles for elytra flaps using the first four-order Fourier terms is as follows:

$$A(t) = \sum_{n=0}^{4} [a_n \cos(nKt) + b_n \sin(nKt)] \tag{1}$$

$$K = \frac{2\pi f c}{2U} \tag{2}$$

where n is integer varying from 0 to 4 and t is dimensionless time; K is the reduced frequency defined by $2fc/2U$; f is the flapping frequency of the elytra with an average value of 67 Hz, and c is the mean chord length (reference length) of the elytra, with an average value of 13.58 mm; U represents the reference velocity of the wing tip of the elytron and is defined by $2\Phi Rf$, which is calculated as 1.12 m/s, where Φ is the flapping wing amplitude of the elytron, which is 18°, and R is the length of the elytron, with an average value of 25.76 mm; coefficients a_n and b_n represent the constant value of the Fourier equation. The coefficients of the Fourier series used to describe the flapping wing motion of the elytra for the three *C. buqueti* samples are shown in Table 1.

3.4 | Numerical simulation of the elytra flapping

The computational domain should be determined in a limited space area during numerical simulation analysis. A smaller airflow simulation environment can simplify the computational task so that boundary disturbances can be considered insignificant to generate reliable simulation results. The setting of the boundaries of a compressible or incompressible fluid is usually determined by the geometry of the object being simulated. The shape and size of the bionic model determine that the flight of *C. buqueti* belongs to an incompressible fluid, and the cuboid is selected as the computational domain. The lengths of approximately 5–10 times wing or 10–20 times mean chord of insects are often taken as the reference to determine the calculation domain [33, 34]. In this study, the dimension of the computational domain is 0.3 m in length (approximately 7 times elytron length), 0.36 m in width (approximately 8 times elytron length) and 0.22 m in height (approximately 5 times elytron length). The ANSYS ICEM-CFD software is used to mesh the geometrical model. A grid of size 265 × 149 × 210 (about 8.3 million) is used for the whole computational domain. The center of the computational domain is meshed into a uniform fine grid. The volume mesh and surface mesh of the computational domain are set as 0.01 m. The elytra mesh in the inner central area of the computational domain is set to 0.0002 m. The time step size in this study is 0.00,001 to ensure stable solutions obtained throughout the simulation.

Reynolds number Re represents the ratio of inertial force to viscous force and is defined as:

$$\mathrm{Re} = \frac{\rho c U}{v} \tag{3}$$

where ρ is the air density, and v is the dynamic viscosity.

CFD computations were conducted using the commercial software Fluent (ANSYS Products 19.0). The Reynolds number is taken as 1041 in the simulation. Numerical simulations were carried out with the help of the 3D incompressible unsteady Navier–Stokes (NS) solver. The surrounding fluid density is constant and incompressible when *C. buqueti* flaps its wings, and a pressure-based solver is used. The air density of standard air condition is 1.225 kg/m^3, and the dynamic viscosity is 1.7894 × 10^{-5} kg/m. According to the experimental observation, the forward flight speed of *C. buqueti* was recorded as 2 m/s. The velocity inlet boundary condition is set at the flow field inlet of the computational domain. At the outlet of flow field, the outlet pressure boundary condition is set. Relative pressure is set as 0 Pa and ambient atmospheric pressure is set as 101,325 Pa. Both the surface of the bionic model and the walls of the computational domain are set as no-slip boundary conditions. In this paper, the elytra are rigid bodies, so the lift and drag coefficients are:

$$C_L = \frac{F_L}{0.5\rho U^2 S_W} \tag{4}$$

$$C_D = \frac{F_D}{0.5\rho U^2 S_W} \tag{5}$$

where C_L and C_D represent the lift coefficient and drag coefficient, respectively. S_W is the projected area of the elytron in the direction of motion, which is 0.276 × 10^{-3} m^2.

To verify the accuracy of the CFD solver used in this paper, a simulation of the flow field around the wing of the *Drosophila* robot was conducted. The robotic wing mimics the wing geometry and flapping motion pattern of *Drosophila* [35] with a wing area of 0.0167 m^2, and a span of 0.25 m, and average wing chord c = 0.0879 m. A non-uniform grid of size 181 × 241 × 181 was used in the

TABLE 1 Constant term of the first four Fourier series in the curve fitting

Samples	a_0	a_1	a_2	a_3	a_4	b_1	b_2	b_3	b_4
$1\theta(t)$	12.283	9.084	−2.585	0.285	0.648	−2.631	−0.856	−0.554	−0.061
$1\phi(t)$	14.669	−16.55	2.08	−0.229	0.027	2.118	0.689	0.281	0.049
$1\alpha(t)$	5.282	0.307	4.994	−0.315	0.183	0.153	−1.589	0.447	−0.03
$2\theta(t)$	11.91	8.811	−2.507	0.276	0.629	−2.552	−0.83	−0.537	−0.059
$2\phi(t)$	14.376	−16.22	2.03	−0.224	−0.026	2.076	0.66	0.275	0.048
$2\alpha(t)$	5.176	0.301	4.894	−0.309	0.179	0.15	1.557	0.438	−0.029
$3\theta(t)$	11.546	8.54	−2.43	0.268	0.609	−2.437	−0.8	−0.521	−0.057
$3\phi(t)$	13.349	−15.06	1.893	−0.21	−0.024	1.927	0.627	0.256	0.044
$3\alpha(t)$	5.02	0.292	4.744	−0.299	0.174	0.145	−1.51	0.425	0.028

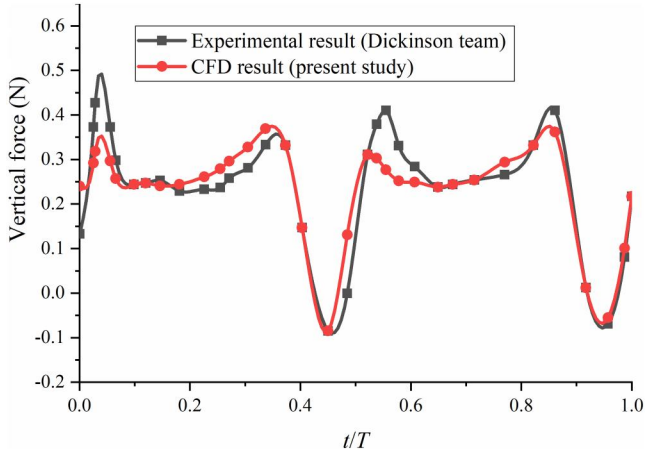

FIGURE 7 Lift production from present study and previous studies on a robotic fruit fly wing

computational domain of $30c \times 30c \times 30c$ to obtain domain-independent results. Figure 7 shows that our simulations are in good agreement with Dickinson's experimental results. This proves that the current numerical methods can accurately predict the aerodynamic forces of the 3D flapping wings.

In order to facilitate the investigation of the pressure distribution of the dorsal surface, the variation law of the surrounding fluid and the effect of the cross-sectional microstructure on the aerodynamic force were conducted. Figure 8 shows the Q-criteria vortex distribution (left column), pressure distribution (middle column) and streamline distribution (right column) during elytra flapping. At the beginning of the downstroke, the elytra rapidly pronate and flap downward, and unstable vortices were observed on the inner surface of the elytra as a result of their generation during the previous upstroke and shedding into the downwash flow. Therefore, a positive pressure region ($t/T = 0$) is formed on the inner surface of the elytra. The continued downstroke of the elytra generates 3D vortex rings, including a leading-edge vortex (LEV), a trailing-edge vortex (TEV) and a wing tip vortex (TV). At the middle of the downstroke ($t/T = 0.25$), the strong LEV generates a negative pressure region on the top surface of the elytra, while the TEV begins to shed towards the wing tip and merge into the TV to form a vortex ring. During the early downstroke ($t/T = 0.55$), the elytra flaps rapidly and encounters positive pressure on the top surface, at which time the new LEV creates a negative pressure region on the inner surface of the elytra. The pressure distribution near the wing base is relatively stable and a little unstable near the wing tip. In order to graphically describe the shedding and attachment of the fluid on the surface of the elytra during the upstroke and downstroke, the streamlines around the elytra are constructed. Streamlines near the leading edge and the wing tip at the mid-downstroke are shown in Figure 8. The spiral streamlines grow in the spanwise direction from the wing base to the wing tip. The streamline near the wing tip bends and joins the TV. The low pressure on the dorsal surface of the elytra can be clearly seen.

The wing surfaces of many insects have corrugations, which result in defined aerodynamic mechanisms such as delayed stall, rotational circulation, clap and fling and wake capture. The corrugated airfoil of insect wing has much better aerodynamic performance over the smooth airfoil [36–38]. The analysis revealed the superiority of the corrugated airfoil over the flat-plate in decreasing the deflection under the applied load [36]. However, there are certain differences between their simulation model and real wings, whose simulation model is zero camber and does not take into account the microstructure of insect wings. The cross-sectional microstructure of elytra of *C. buqueti* obtained by SEM is a cambered morphology with local corrugations. With the increase of the angle of attack, the fluid separates around the elytra, but the corrugations of the leading edge of the elytra prevents rapid fluid separation. The corrugations located near the leading edge may be one of the main contributors to the lift generated by elytra flapping. The lift coefficient and drag coefficient curves of elytra in one flapping wing cycle are shown in Figure 9. The calculated average lift coefficient and drag coefficient are 0.152 and 0.029, respectively. In a flapping cycle, the flapping of elytra produces a small drag ($F_D = 0.006$ g) and average vertical force ($F_L = 0.031$ g). The cambered airfoil structure of the elytra has advantages in terms of aerodynamic performance because it generates a

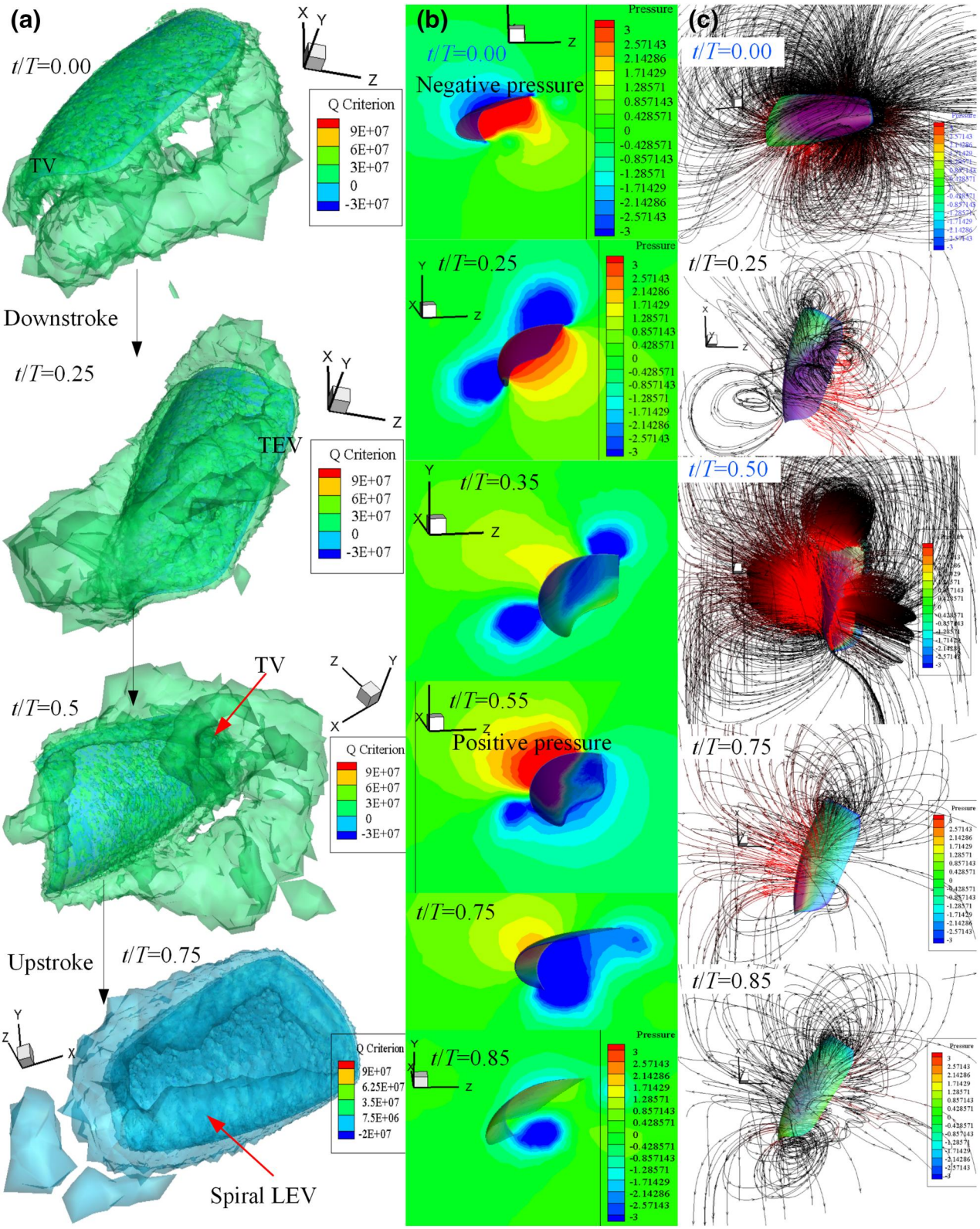

FIGURE 8 Isometric views of fluid changes around the elytra. (a) Time course of vortex development, visualised by the Q criterion, (b) surface pressure distribution, and (c) streamlines distribution on the elytron surface at some typical time steps

high vertical force value ($t/T = 0.0$) at the beginning of the downstroke. Therefore, the elytra of *C. buqueti* can not only has the functions of protecting the hind wings and promoting the folding and unfolding of the hind wings but also can be coupled with the flapping of the hind wings to generate useful aerodynamic force.

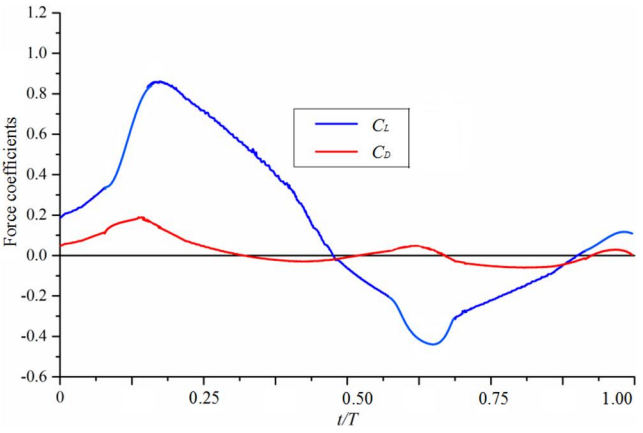

FIGURE 9 Aerodynamic coefficients of the elytra of the Cyrtotrachelus buqueti flapping

4 | CONCLUSION

In this paper, the functional morphology of elytra of *C. buqueti* was investigated by high-speed camera system, SEM, 3D scanning and reverse reconstruction technology and CFD simulation technology. A modified direct linear transformation algorithm is used to analyse the variation characteristics of the elytra flapping. It is found that there is a non-negligible Euler angle change in the passive motion of the elytra, and the flapping trajectory is a double figure-eight pattern. The SEM observation of the microstructure of the ventral side of the elytra shows that the sharp micro protrusion plays a special role in the folding and unfolding, self-locking after unfolding and anti-collision after falling. Accurate 3D models of elytra were obtained by 3D scanners and inverse reconstruction techniques. The aerodynamic characteristics of the elytra flapping were investigated based on a CFD simulator. During the elytra flap, a vertical force of 0.94% of the beetle's body weight is generated, and vortex ring phenomena such as LEV, TEV, and TV appear. Therefore, the elytra of *C. buqueti* not only have the function of protecting the hind wings and promoting the folding and unfolding of the hind wings but also can be coupled with the flapping of the hind wings to generate useful aerodynamic force. Furthermore, the flapping trajectory of the elytra suggests that *C. buqueti* may utilise the delayed stall of the LEV, clap and fling, wing-wing coupling, and the figure-eight motion pattern to generate unconventional aerodynamic forces.

ACKNOWLEDGEMENTS

This work was supported by the Natural Science Foundation of Jiangsu Higher Education Institutions of China (Grant Nos. 21KJD460002), the Suqian Sci&Tech Program of China (Grant Nos. K202115), and the Research and Design Innovation Team of Lightweight Rotor Pump of Suqian University (Grant Nos. 2021td7).

CONFLICT OF INTEREST

The authors declare no potential conflict of interest.

DATA AVAILABILITY STATEMENT

The data presented in this study are available on request from the corresponding author.

ORCID

Xin Li https://orcid.org/0000-0002-4986-5035
Yu Zheng https://orcid.org/0000-0003-2140-7582

REFERENCES

1. Le, T.Q., et al.: Numerical investigation of the aerodynamic characteristics of a hovering Coleopteran insect. J. Theor. Biol. 266(4), 485–495 (2011). https://doi.org/10.1016/j.jtbi.2010.07.013
2. Wan, H., Dong, H., Gai, K.: Computational investigation of cicada aerodynamics in forward flight. J. R. Soc. Interface 12(102), 20141116 (2015). https://doi.org/10.1098/rsif.2014.1116
3. Cheng, X., Sun, M.: Wing-kinematics measurement and aerodynamics in a small insect in hovering flight. Sci. Rep. 6(1)25706 (2016). https://doi.org/10.1038/srep25706
4. Li, C., Dong, H.: Wing kinematics measurement and aerodynamics of a dragonfly in turning flight. Bioinspiration Biomimetics 12(2), 026001 (2017). https://doi.org/10.1088/1748-3190/aa5761
5. Meng, X., Liu, Y., Sun, M.: Aerodynamics of ascending flight in fruit flies. J. Bionic Engg. 14(1), 75–87 (2017). https://doi.org/10.1016/S1672-6529(16)60379-7
6. Xiang, J., et al.: Aerodynamic performance of the locust wing in gliding mode at low Reynolds number. J. Bionic Engg. 13(2), 249–260 (2016). https://doi.org/10.1016/S1672-6529(16)60298-6
7. Ribak, G., Barkan, S., Soroker, V.: The aerodynamics of flight in an insect flight-mill. PLoS One 12(11), e0186441 (2017). https://doi.org/10.1371/journal.pone.0186441
8. Lee, B., Park, H., Kim, S.T.: Three-dimensional wing behaviors of a rhinoceros beetle during takeoff flights. J. Mech. Sci. Technol. 29(12), 5281–5288 (2015). https://doi.org/10.1007/s12206-015-1130-x
9. Ma, K.Y., et al.: Controlled flight of a biologically inspired, insect-scale robot. Science. 340(6132), 603–607 (2013). https://doi.org/10.1126/science.1231806
10. Bao, X., et al.: Design and fabrication of insect inspired composite wings for MAV application using MEMS technology. J. Micromech. Microeng. 21(12), 125020 (2011). https://doi.org/10.1088/0960-1317/21/12/125020
11. Shen, H., et al.: Structure and aerodynamic characteristics of a coaxial quad-wing flapper. P I Mech. Eng. G J. Aer. 235(10), 1197–1210 (2020). https://doi.org/10.1177/0954410020967546
12. Chen, Y., et al.: A biologically inspired, flapping-wing, hybrid aerial-aquatic microrobot. Sci. Robot. 2(11), eaao5619 (2017). https://doi.org/10.1126/scirobotics.aao5619
13. Karásek, M., et al.: A tailless aerial robotic flapper reveals that flies use torque coupling in rapid banked turns. Science. 361(6407), 1089–1094 (2018). https://doi.org/10.1126/science.aat0350
14. Sitorus, P.E., et al.: The role of elytra in beetle flight: I. Generation of quasi-static aerodynamic forces. J. Bionic Engg. 7(4), 354–363 (2010). https://doi.org/10.1016/S1672-6529(10)60267-3
15. Johansson, L.C., et al.: Elytra boost lift, but reduce aerodynamic efficiency in flying beetles. J. R. Soc. Interface 9(75), 2745–2748 (2012). https://doi.org/10.1098/rsif.2012.0053
16. Truong, T.V., et al.: Flow visualization of rhinoceros beetle (*Trypoxylus dichotomus*) in free flight. J. Bionic Engg. 9(3), 304–314 (2012). https://doi.org/10.1016/S1672-6529(11)60127-3
17. Le, T.Q., et al.: Two- and three-dimensional simulations of beetle hind wing flapping during free forward flight. J. Bionic Engg. 10(3), 316–328 (2013). https://doi.org/10.1016/S1672-6529(13)60227-9
18. Le, T.Q., et al.: How could beetle's elytra support their own weight during forward flight. J. Bionic Engg. 11(4), 529–540 (2014). https://doi.org/10.1016/S1672-6529(14)60065-2
19. Prasath, N.G., et al.: Numerical simulation of biology-inspired beetle wings at various flying conditions. In: 12th International Energy

Conversion Engineering Conference (2014). https://doi.org/10.2514/6.2014-3763
20. Xiang, J., et al.: Effects of micro-structure on aerodynamics of *coccinella septempunctata* elytra (ladybird) in forward flight as assessed via electron microscopy. Micron 102, 21–34 (2017). https://doi.org/10.1016/j.micron.2017.08.003
21. Phan, H.V., Au, T.K.L., Park, H.C.: Clap-and-fling mechanism in a hovering insect-like two-winged flapping-wing micro air vehicle. R. Soc. Open Sci. 3(12), 160746 (2016). https://doi.org/10.1098/rsos.160746
22. Phan, H.V., Park, H.C.: Mechanisms of collision recovery in flying beetles and flapping-wing robots. Science. 370(6521), 1214–1219 (2020). https://doi.org/10.1126/science.abd3285
23. Li, X., Guo, C., Li, L.: Functional morphology and structural characteristics of the hind wings of the bamboo weevil *Cyrtotrachelus buqueti* (Coleoptera, Curculionidae). Anim Cells Syst. 23(2), 143–153 (2019). https://doi.org/10.1080/19768354.2019.1592020
24. Li, X., Guo, C.: Microstructure and material properties of hind wings of a bamboo weevil *Cyrtotrachelus buqueti* (Coleoptera: Curculionidae). Microsc. Res. Tech. 82(7), 1102–1113 (2019). https://doi.org/10.1002/jemt.23258
25. Li, X., Guo, C.: Structural characteristics analysis of the hind wings in a bamboo weevil (*Cyrtotrachelus buqueti*). IET Nanobiotechnol. 13(8), 850–856 (2019). https://doi.org/10.1049/iet-nbt.2018.5409
26. Li, X., Guo, C.: Wing-kinematics measurement and flight modelling of the bamboo weevil *C. buqueti*. IET Nanobiotechnol. 14(1), 53–58 (2020). https://doi.org/10.1049/iet-nbt.2019.0261
27. Li, X., et al.: Design of bionic foldable wing mimicking the hind wings of the *C. Buqueti* bamboo weevil. J. Mech. Des. 143(8), 1–15 (2021). https://doi.org/10.1115/1.4049340
28. Hedrick, T.L.: Software techniques for two-and three-dimensional kinematic measurements of biological and biomimetic systems. Bioinspiration Biomimetics 3(3), 034001 (2008). https://doi.org/10.1088/1748-3182/3/3/034001
29. Koehler, C., et al.: 3D reconstruction and analysis of wing deformation in free-flying dragonflies. J. Exp. Biol. 215(17), 3018–3027 (2012). https://doi.org/10.1242/jeb.069005
30. Srygley, R.B., Thomas, A.L.: Unconventional lift-generating mechanisms in free-flying butterflies. Nature. 420(6916), 660–664 (2002). https://doi.org/10.1038/nature01223
31. Chen, Y., et al.: Dragonfly (*Sympetrum flaveolum*) flight: kinematic measurement and modelling. J. Fluid Struct. 40, 115–126 (2013). https://doi.org/10.1016/j.jfluidstructs.2013.04.003
32. Yang, S., Zhang, W.: Numerical analysis of the three-dimensional aerodynamics of a hovering rufous hummingbird (*Selasphorus rufus*). Acta Mech. Sin. 31(6), 931–943 (2015). https://doi.org/10.1007/s10409-015-0450-5
33. Aono, H., Liang, F., Liu, H.: Near- and far-field aerodynamics in insect hovering flight: an integrated computational study. J. Exp. Biol. 211(2), 239–257 (2008). https://doi.org/10.1242/jeb.008649
34. Sun, J., et al.: A simulation of the flight characteristics of the deployable hindwings of beetle. J. Bionic Engg. 14(2), 296–306 (2017). https://doi.org/10.1016/S1672-6529(16)60392-X
35. Dickinson, M.H., Lehmann, F.O., Sane, S.P.: Wing rotation and the aerodynamic basis of insect flight. Science. 284(5422), 1954–1960 (1999). https://doi.org/10.1126/science.284.5422.1954
36. Nassar, M., Elsayed, K., Abdelrahman, M.M.: Aerodynamic study of the corrugated airfoil at ultra-low Reynolds number. Adv. Mech. Eng. 11(10), 1–18 (2019). https://doi.org/10.1177/1687814019884164
37. Meng, X.G., Xu, L., Sun, M.: Aerodynamic effects of corrugation in flapping insect wings in hovering flight. J. Exp. Biol. 214(3), 432–444 (2011). https://doi.org/10.1242/jeb.046375
38. Meng, X.G., Sun, M.: Aerodynamic effects of wing corrugation at gliding flight at low Reynolds numbers. Phys. Fluids 25(7), 071905 (2013). https://doi.org/10.1063/1.4813804

How to cite this article: Li, X., Zheng, Y.: Functional characteristics of the rigid elytra in a bamboo weevil beetle *Cyrtotrachelus buqueti*. IET Nanobiotechnol. 16(7-8), 273–283 (2022). https://doi.org/10.1049/nbt2.12095